

Chiral plasma instability and inverse cascade from nonequilibrium left-handed neutrinos in core-collapse supernovae

Jin Matsumoto¹, Naoki Yamamoto¹, and Di-Lun Yang²

¹*Department of Physics, Keio University, Yokohama 223-8522, Japan*

²*Institute of Physics, Academia Sinica, Taipei, 11529, Taiwan*

We show that the backreaction of left-handed neutrinos out of equilibrium on the matter sector induces an electric current proportional to a magnetic field even without a chiral imbalance for electrons in core-collapse supernovae. We derive the transport coefficient of this effect based on the recently formulated chiral radiation transport theory for neutrinos. This chiral electric current generates a strong magnetic field via the so-called chiral plasma instability, which could provide a new mechanism for the strong and stable magnetic field of magnetars. We also numerically study the physical origin of the inverse cascade of the magnetic energy in the magnetohydrodynamics including this current. Our results indicate that incorporating the chiral effects of neutrinos would drastically modify the hydrodynamic evolutions of supernovae, which may also be relevant to the explosion dynamics.

I. INTRODUCTION AND SUMMARY

Following the theoretical suggestion by Lee and Yang [1], Wu and collaborators experimentally discovered that the weak interaction violates the parity symmetry, one of the most fundamental symmetries in nature [2]. In this experiment, a polarized ^{60}Co in the external magnetic field at low temperature decays into ^{60}Ni by emitting an electron (and an antineutrino) via the weak interaction. The observation that the electron is preferentially emitted into the direction opposite to the magnetic field shows that the weak interaction violates parity symmetry. Later, it was also confirmed that neutrinos are only left-handed within the Standard model (SM) of particle physics [3].

On the other hand, this important feature of neutrinos is missed in the conventional radiation transport theory used in numerical simulations of core-collapse supernovae; see, e.g., Refs. [4–9]. Only recently, based on the idea of the relevance of the chirality of neutrinos in the hydrodynamic evolutions of supernovae [10], the radiation transport theory incorporating this effect was constructed systematically from the underlying SM [11]. Using this chiral radiation transport theory, it was also found that a magnetic field induces nonequilibrium corrections on the neutrino energy-momentum tensor and neutrino number current [12]; see also Eqs. (1) and (2) below.

In this paper, we show that backreaction of these nonequilibrium left-handed neutrinos on the matter sector induces an electric current proportional to the magnetic field in core-collapse supernovae. We derive this transport coefficient based on our previous works [11, 12].

As this chiral electric current generates a strong magnetic field via the so-called chiral plasma instability (CPI) [13, 14], this could provide a new mechanism for the strong and stable magnetic field of magnetars. We also numerically study the physical reason why the subsequent magnetohydrodynamic (MHD) evolutions including this current exhibit the inverse cascade of the magnetic field.

Although neutrinos fully out of equilibrium would provide potentially dominant contributions, backreaction from neutrinos near equilibrium could at least qualitatively and perhaps even quantitatively lead to non-negligible effects on the evolution of the matter sector as will be shown here. Whether our new mechanism operates at a more quantitative level should be tested by numerical applications of the chiral radiation transport theory for neutrinos [11] in the future. This direction would also be important to study the impacts of the chiral effects of neutrinos on the explosion dynamics.

Throughout this paper, we use the natural units $\hbar = c = k_B = 1$. The electric charge e is absorbed into the definition of electromagnetic fields.

II. CHIRAL ELECTRIC CURRENT INDUCED BY NONEQUILIBRIUM NEUTRINOS

In Ref. [12], it was shown based on the chiral transport theory for neutrinos [11] that there are additional contributions from nonequilibrium neutrinos to the neutrino current j_ν^i and neutrino momentum density T_ν^{i0} propor-

tional to the magnetic field \mathbf{B} :

$$\Delta j_\nu^i = -\kappa(\nabla \cdot \mathbf{v})B^i, \quad (1)$$

$$\Delta T_\nu^{i0} = -\mu_\nu \kappa (\nabla \cdot \mathbf{v}) B^i, \quad (2)$$

where μ_ν is the neutrino chemical potential and \mathbf{v} is the fluid velocity. Here and below, ΔO denotes the contribution of chiral effects to a physical quantity O . The coefficient κ can be computed analytically under certain approximations as [12]

$$\kappa = \frac{1}{72\pi M G_F^2 (g_V^2 + 3g_A^2)} \frac{e^{2\beta(\mu_n - \mu_p)}}{n_n - n_p}, \quad (3)$$

where M is the mass of nucleons, G_F is the Fermi constant, $g_{V,A}$ are the nucleon vector/axial charges, μ is the chemical potential, n is the number density (with the subscripts ‘‘p’’ and ‘‘n’’ denoting protons and neutrons, respectively), and β is the inverse temperature. Here, we note the relation $\Delta T_\nu^{i0} = \mu_\nu \Delta j_\nu^i$. This can be naturally understood as the neutrino momentum density (which is equal to the neutrino energy current ΔT_ν^{0i}) being given by the neutrino number current multiplied by the neutrino energy around the Fermi surface.

From the momentum conservation law, the matter sector receives momentum kick from neutrinos as

$$\Delta T_e^{i0} = -\Delta T_\nu^{i0}, \quad (4)$$

where T_e^{i0} is the momentum density of electrons. Here, we ignored the nucleon recoil in the neutrino scattering consistently, which we also used to derive Eqs. (1) and (2) when taking the leading-order contribution in the expansion in terms of $|\mathbf{p}|/M$ (with \mathbf{p} the momentum transfer) [12]. We also assume a relation between the current and momentum density for electrons similar to the one for neutrinos above, $\Delta T_e^{i0} = \mu_e \Delta j_e^i$, where μ_e is the electron chemical potential and j_e^i is the electron number current. The electric current of electrons is given by $J_e^i = -j_e^i$.

Combining these relations together, we obtain an electron current proportional to the magnetic field:

$$\Delta J_e^i = \xi_B B^i, \quad \xi_B = -\kappa(\nabla \cdot \mathbf{v}) \frac{\mu_\nu}{\mu_e}. \quad (5)$$

Note that this is different from the so-called chiral magnetic effect (CME) [15–17] in that it occurs even without the chirality imbalance of electrons itself. Physically, this can be understood similarly to the Wu experiment showing the correlation between the direction of the emitted antineutrinos/electrons and the direction of the magnetic field. Our result (5), which we have derived here for the first time based on the SM, can be seen as a nonequilibrium many-body manifestation of the microscopic parity

violation. Note that in this mechanism, damping the chirality imbalance of electrons due to the finite electron mass is irrelevant unlike the scenario in Refs. [18, 19].¹

Taking $n_n - n_p \sim 0.1 \text{ fm}^{-3}$, $\mu_n - \mu_p \sim 100 \text{ MeV}$, $\mu_\nu \sim \mu_e \sim 100 \text{ MeV}$, $T \sim 10 \text{ MeV}$, $|\mathbf{v}| \sim 0.01$, and the typical length scale of the system, $\ell \sim 10 \text{ km}$, we have $\xi_B \sim 10 \text{ MeV}$.² While ξ_B here is not associated with the chirality imbalance of electrons, they have the same quantum number. From the comparison of Eq. (5) with the expression of the CME, $\mathbf{J}_{\text{CME}} = \mu_5 \mathbf{B}/(2\pi^2)$ [15–17], we may define an ‘‘effective chiral chemical potential’’ $\mu_{5,\text{eff}} = 2\pi^2 \xi_B \sim 100 \text{ MeV}$. Assuming $\mu_e \gg T$, one can also relate the coefficient ξ_B to the ‘‘effective chiral charge’’ $n_{5,\text{eff}}$ as

$$\xi_B = \frac{1}{4} \left(\frac{3}{\pi^4} \right)^{1/3} [(n_e + n_{5,\text{eff}})^{1/3} - (n_e - n_{5,\text{eff}})^{1/3}], \quad (6)$$

where n_e is the number density of electrons.

In general, the backreaction leads to the modifications of the total energy current and charge current (except for other dissipative terms) as

$$T_{\text{mat}}^{0i} = (\epsilon + P)u^i - \mu_e \xi_B B^i, \quad (7)$$

$$J^i = (n_p - n_e)u^i + \xi_B B^i. \quad (8)$$

Here, T_{mat}^{0i} and J^i denote the energy current of the matter sector and total electric current, respectively, with ϵ being the energy density, P the pressure, and u^μ the fluid four velocity. It is however more convenient to work on the hydrodynamic equations in the Landau frame by redefining a fluid velocity \tilde{u}^μ (such that $T^{0i} \propto \tilde{u}^i$) as

$$\tilde{u}^\mu = u^\mu - \frac{\mu_e \xi_B}{\epsilon + P} B^\mu, \quad (9)$$

where $B^\mu = \epsilon^{\mu\nu\alpha\beta} u_\nu F_{\alpha\beta}/2$ is the magnetic field defined in the fluid rest frame, with $F_{\alpha\beta}$ as the field strength of the electromagnetic field. Consequently, we have

$$T_{\text{mat}}^{0i} = (\epsilon + P)\tilde{u}^i, \quad (10)$$

$$J^i = (n_p - n_e)\tilde{u}^i + \left[1 - \frac{(n_e - n_p)\mu_e}{\epsilon + P} \right] \xi_B B^i. \quad (11)$$

When assuming the local charge neutrality $n_e = n_p$, we reproduce the result (5) also in the Landau frame.

¹ One might also suspect that the nonzero neutrino mass m_ν can cause the chirality flipping of neutrinos. However, such flipping is suppressed by an additional factor involving $m_\nu/\mu_\nu \lesssim 10^{-8}$ compared with the weak process without chirality flipping.

² One should note that this value is sensitive to the choice of the parameters, and it should be rather regarded as the upper bound for ξ_B , similarly to the discussion in Ref. [12].

III. HELICAL MAGNETIC FIELD GENERATED BY THE CHIRAL PLASMA INSTABILITY

As argued in Ref. [10], any electric current of the form $\Delta\mathbf{J} = \xi_B\mathbf{B}$ induces the CPI [13, 14], although the origin of ξ_B here is different from previous studies [10, 14, 18–22].

To make our paper self-contained, we here summarize several relations regarding the CPI; see, e.g., Ref. [23]. Inserting the perturbation of the form $\delta\mathbf{B} \propto e^{\sigma t + i\mathbf{k}\cdot\mathbf{x}}$ (with σ being the growth rate of the CPI) into Maxwell equations with the current $\Delta\mathbf{J} = \xi_B\mathbf{B}$, the linear analysis leads to the dispersion relation

$$\sigma = \eta k(\xi_B - k), \quad (12)$$

where $k \equiv |\mathbf{k}|$ is the wave number. This σ is positive as long as $0 < k < k_{\text{crit}}$ with $k_{\text{crit}} \equiv \xi_B$, and the corresponding critical length is

$$\lambda_{\text{crit}} \equiv \frac{2\pi}{k_{\text{crit}}} = \frac{2\pi}{\xi_B}. \quad (13)$$

One also finds that σ becomes maximum when $k = \xi_B/2 \equiv k_{\text{CPI}}$ and the corresponding time and length scales are

$$\tau_{\text{CPI}} = \frac{4}{\eta\xi_B^2}, \quad \lambda_{\text{CPI}} \equiv \frac{2\pi}{k_{\text{CPI}}} = \frac{4\pi}{\xi_B}, \quad (14)$$

respectively.

We now provide an estimate for the magnetic field generated by this CPI. Although the origin of ξ_B is different, the argument here is similar to Ref. [18]. In the ideal Fermi gas approximation, the additional energy density due to $\mu_{5,\text{eff}}$ is

$$\Delta\epsilon = \frac{1}{4\pi^2}(\mu_{5,\text{eff}}^4 + 6\mu_{5,\text{eff}}^2\mu_e^2). \quad (15)$$

Assuming this whole energy is converted to that of the magnetic field by the CPI, $B_{\text{CPI}}^2/2$, one can estimate the maximum magnetic field as

$$B_{\text{CPI}} \sim \mu_{5,\text{eff}}^2 \sim 10^{18} \text{ Gauss}. \quad (16)$$

We will also verify this estimate by numerical simulations of the MHD below (see Fig. 1). Here, the strong magnetic field is generated from the energy temporarily stored in neutrinos, as can be seen from the relation $\mu_{5,\text{eff}} \propto \mu_\nu$. This new mechanism could potentially explain the origin of the gigantic magnetic field of magnetars. Note that unlike the conventional mechanism for magnetars, the magnetic field generated by the CPI possesses a nonzero magnetic helicity that characterizes the linking structure of poloidal and toroidal magnetic fields [18]. This ensures the stability of the resulting strong magnetic field.

In this estimate of the maximum magnetic field, we adopt several optimistic assumptions. To what extent this mechanism is efficient in core-collapse supernovae should be numerically checked by the chiral radiation transport theory for neutrinos in Ref. [11].

IV. INVERSE CASCADE IN CHIRAL MHD

In Ref. [23], numerical simulations of the MHD with the current $\Delta\mathbf{J} = \xi_B\mathbf{B}$ (chiral MHD) in the protoneutron star were performed. Consequently, the CPI and the subsequent inverse cascade of the magnetic field in the late nonlinear phase for $8 \times 10^{-4} \leq \xi_{B,\text{ini}} \leq 2 \times 10^{-2}$ (in the units of $100 \text{ MeV} = 1$) are observed; see also Refs. [24, 25] for the inverse cascade of the chiral MHD in the context of the early Universe. As we discussed above, in this paper we provide a new mechanism for ξ_B , which leads to a rather larger value $\xi_B \sim 0.1$. Although the chiral MHD with this value has not been tested previously, one expects that this would also lead to the inverse cascade of the magnetic field. More generally, one can ask the physical origin of the inverse cascade of the magnetic field in the present system unlike the usual MHD. To address this question, we extend the work [23] in somewhat wider range of the initial value of ξ_B including $\xi_B \sim 0.1$ ($10^{-5} \leq \xi_{B,\text{ini}} \leq 10^{-1}$) and clarify the origin of the inverse cascade.

The governing chiral MHD equations are given in Ref. [23]. For the present numerical simulations, we rewrite these equations into a conservative form using Maxwell equations as

$$\frac{\partial \rho}{\partial t} + \nabla \cdot (\rho\mathbf{v}) = 0, \quad (17)$$

$$\frac{\partial}{\partial t}(\rho\mathbf{v}) + \nabla \cdot \left[\rho\mathbf{v}\mathbf{v} - \mathbf{B}\mathbf{B} + \left(P + \frac{B^2}{2} \right) \mathbf{I} \right] = \mathbf{S}, \quad (18)$$

$$\begin{aligned} \frac{\partial}{\partial t} \left(\frac{1}{2}\rho v^2 + \frac{1}{\Gamma-1}P + \frac{B^2}{2} \right) + \nabla \cdot \left[\left(\frac{1}{2}\rho v^2 + \frac{\Gamma}{\Gamma-1}P \right) \mathbf{v} \right. \\ \left. + \mathbf{E} \times \mathbf{B} \right] = \mathbf{S} \cdot \mathbf{v} - \Delta\mathbf{J} \cdot \mathbf{E}, \quad (19) \end{aligned}$$

$$\frac{\partial \mathbf{B}}{\partial t} = \nabla \times (\mathbf{v} \times \mathbf{B}) + \eta \nabla^2 \mathbf{B} + \eta \nabla \times (\xi_B \mathbf{B}), \quad (20)$$

$$\frac{\partial n_{5,\text{eff}}}{\partial t} = \frac{1}{2\pi^2} \mathbf{E} \cdot \mathbf{B}. \quad (21)$$

Equations (17)–(20) correspond to the mass conservation, momentum conservation, energy conservation, and induction equation, respectively. Here, ρ is the rest-mass density, \mathbf{E} is the electric field, η is the resistivity, Γ is the ratio of specific heats (which we assume to be the value

of the ideal gas, $\Gamma = 5/3$), \mathbf{I} is the unit matrix, and

$$\mathbf{S} = \rho\nu\nabla^2\mathbf{v} + \frac{1}{3}\rho\nu\nabla(\nabla\cdot\mathbf{v}), \quad (22)$$

with ν as the viscosity. To describe the evolution of $n_{5,\text{eff}}$, we also postulate Eq. (21) similar to the chiral anomaly relation that stands for the helicity conservation (see, e.g., Ref. [10]). In Eq. (21), the advection, diffusion, chiral separation effect, and cross helicity are ignored for simplicity as in Ref. [23].

In fact, the total helicity conservation is derived from the spatial integration of Eq. (21) as

$$\frac{dH_{\text{tot}}}{dt} = 0, \quad H_{\text{tot}} \equiv N_{5,\text{eff}} + \frac{H_{\text{mag}}}{4\pi^2}, \quad (23)$$

where

$$N_{5,\text{eff}} \equiv \int d^3\mathbf{x} n_{5,\text{eff}}, \quad H_{\text{mag}} \equiv \int d^3\mathbf{x} \mathbf{A} \cdot \mathbf{B}, \quad (24)$$

are the global effective chiral charge and the magnetic helicity, respectively. Here, \mathbf{A} is the vector potential defined by $\mathbf{B} = \nabla \times \mathbf{A}$.

One can eliminate the electric field in the governing equations above through the modified Ohm's law including the chiral current,

$$\mathbf{E} + \mathbf{v} \times \mathbf{B} = \eta(\mathbf{J} - \Delta\mathbf{J}), \quad (25)$$

where $\mathbf{J} = \nabla \times \mathbf{B}$ is the total electric current.

As for the approximate Riemann solver, the HLLD scheme [26] is used in our code to solve chiral MHD equations (17)–(21) in a conserved form. We use a MUSCL-type interpolation method to attain second-order accuracy in space while the temporal accuracy obtains second order by using Runge-Kutta time integration. In addition, the constrained transport method is implemented in our code to guarantee the condition $\nabla \cdot \mathbf{B} = 0$ [27]. Our numerical setups are almost same as those in Ref. [23] except for several physical parameters. We adopt $\nu = 0.01$ and $\eta = 1$ in all our numerical runs. The initial value $\xi_{B,\text{ini}}$ (listed in Table I) varies from 10^{-1} to 10^{-5} among models.

In our numerical runs, we resolve λ_{crit} in Eq. (13) by 10 grid points and take the grid size $\Delta = \lambda_{\text{crit}}/10$. The number of grid points in our simulations is fixed ($N^3 = 128^3$). However, the size of the calculation domain, $L = N \times \Delta$, is changed between models because of the variation of $\xi_{B,\text{ini}}$ in models. The typical timescale of the CPI, τ_{CPI} , and L in each model are also listed in Table I.³

TABLE I. Summary of the simulation runs.

| Name | L | $\xi_{B,\text{ini}}$ | τ_{CPI} |
|---------|-----------------|----------------------|---------------------|
| model 1 | 8×10^2 | 10^{-1} | 4×10^2 |
| model 2 | 8×10^3 | 10^{-2} | 4×10^4 |
| model 3 | 8×10^4 | 10^{-3} | 4×10^6 |
| model 4 | 8×10^5 | 10^{-4} | 4×10^8 |
| model 5 | 8×10^6 | 10^{-5} | 4×10^{10} |

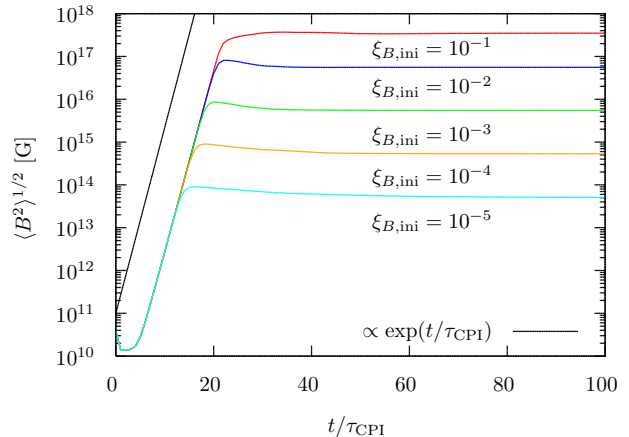


FIG. 1. Time evolution of $\langle B^2 \rangle^{1/2}$.

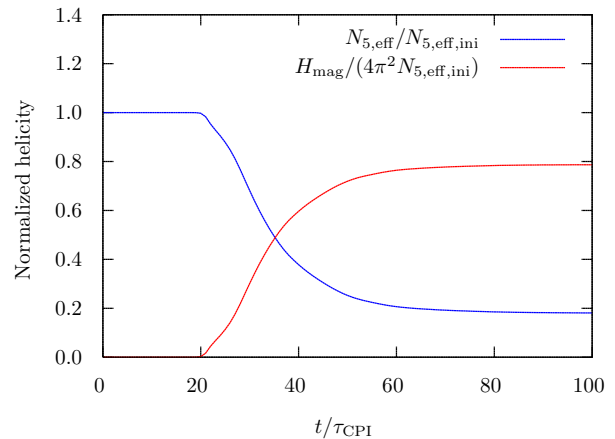


FIG. 2. Time evolution of normalized helicity in model 1.

³ As global simulations with the macroscopic length ℓ are computa-

tionally too expensive with the current numerical resources, here we instead perform local simulations with the size of the small domain, e.g., $L \simeq 1.6 \times 10^{-12}$ m for model 1, by extrapolating the near-equilibrium regime for neutrinos.

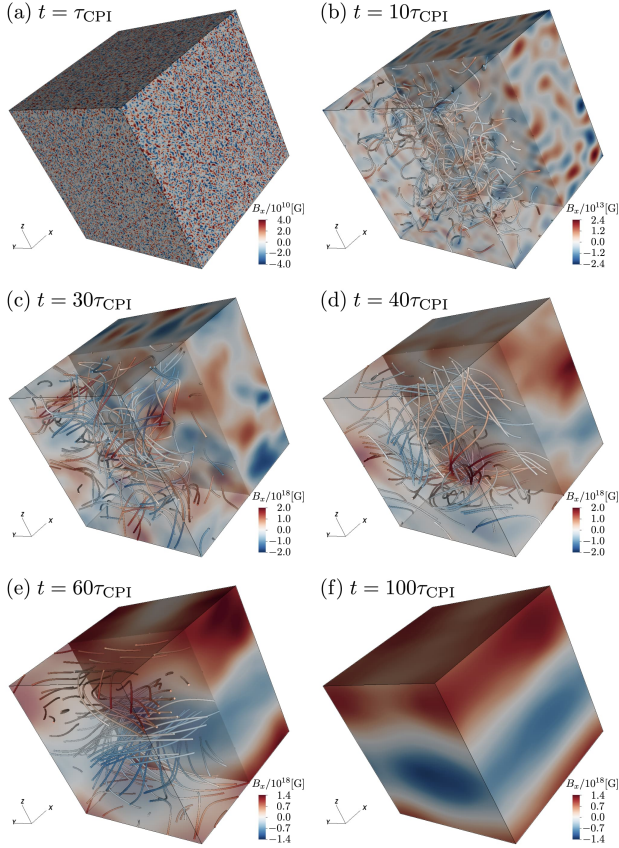


FIG. 3. Time evolution of 3D visualization of B_x and magnetic field lines in model 1. Panels (a), (b), (c), (d), (e), and (f) correspond to the time $t/\tau_{\text{CPI}}=1, 10, 30, 40, 60,$ and $100,$ respectively.

Figure 1 shows the temporal evolution of the strength of the volume-averaged magnetic field $\langle B^2 \rangle^{1/2}$, where the volume average of a physical quantity O is defined by

$$\langle O \rangle = \frac{1}{V} \int d^3\mathbf{x} O, \quad V \equiv \int d^3\mathbf{x}. \quad (26)$$

The analytically predicted temporal evolution of the magnetic field due to the growth of the CPI ($\propto e^{t/\tau_{\text{CPI}}}$) is also shown by a black solid line, for reference. In all models, the growth rate of the magnetic field in the early phase of simulation runs after the relaxation of the initial perturbation of the magnetic field has good agreement with the linear analysis of the CPI. In the later phase of the simulations, the amplification of the magnetic field due to the CPI is saturated.

The magnetic helicity H_{mag} is drastically generated in the nonlinear phase. The temporal evolutions of H_{mag} and $N_{5,\text{eff}}$ for model 1 are plotted by red and blue lines in Fig. 2. The vertical axis is normalized by the initial effective chiral charge, $N_{5,\text{eff},\text{ini}}$. From the point of view

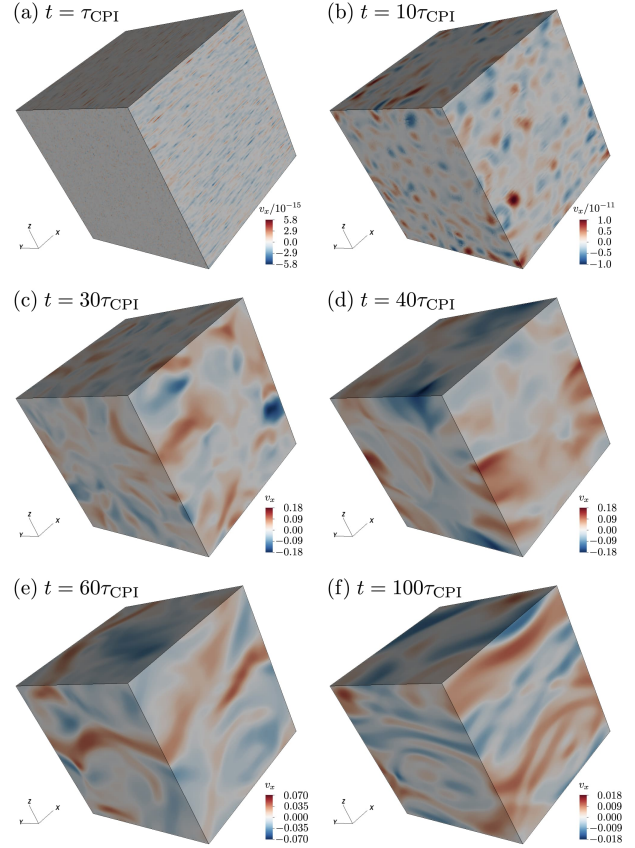


FIG. 4. Temporal evolution of 3D visualization of v_x in model 1. Time in each panel is the same as that in Fig. 3.

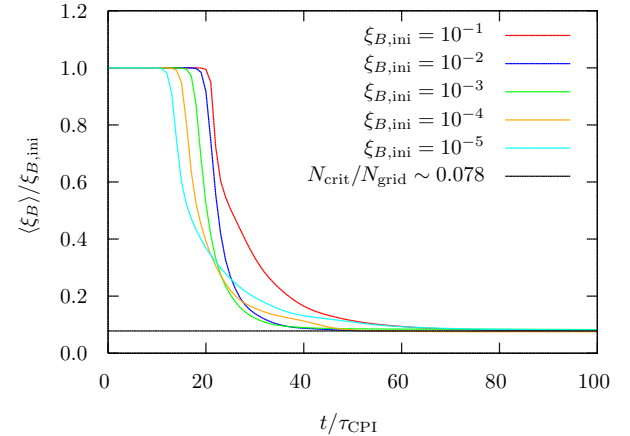


FIG. 5. Time evolution of $\langle \xi_B \rangle$.

of the conservation of the total helicity, the decrease of $N_{5,\text{eff}}$ compensates for the increase of H_{mag} . As discussed later, the saturation level of $N_{5,\text{eff}}$, which is related to ξ_B by Eq. (6), depends on L .

The inverse cascade of the magnetic energy and fluid

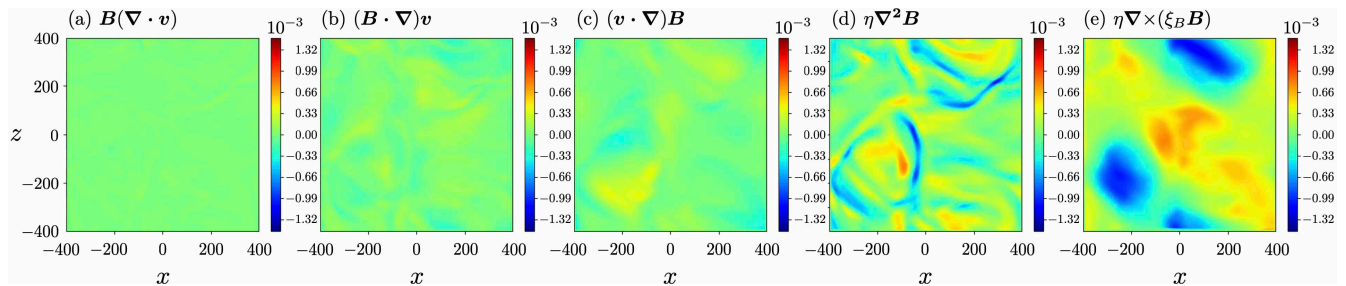


FIG. 6. Comparison of the terms in the induction equation at $t = 40\tau_{\text{CPI}}$ for model 1.

kinetic energy is also observed in all our models. Figure 3 shows several time snapshots of 3D rendering of B_x and magnetic field lines in the whole calculation domain of model 1 ($\xi_{B,\text{ini}} = 10^{-1}$) listed in Table I. In Figs. 3(a) and 3(f), only B_x is illustrated. In Figs. 3(b)–3(e), the magnetic field lines are visualized in the negative x region and the colors of the magnetic field lines indicate the strength of B_x . The 2D distribution of B_x on the surface of the calculation box in the negative x region is made transparent to depict the magnetic field lines. We can see that the correlation length of B_x (the size of the red and blue regions) becomes larger over time. The final length scale of B_x becomes comparable to L as shown in Fig. 3(f). This feature can be checked in all models listed in Table I. In addition, the inverse cascade of the fluid kinetic energy in model 1 is confirmed in Fig. 4. The box size and time in each panel in this figure are the same as those in Fig. 3. While v_x has small-scale structures in the linear phase [Fig. 4(b)], it gradually organizes large-scale structures in the nonlinear phase [Figs. 4(c)–4(f)].

Let us now discuss the physical reason why the magnetic field exhibits the inverse cascade in this system. In the linear phase of our simulation runs, the CPI with the typical wavelength λ_{CPI} is developed as shown in Fig. 3(b). In this phase, the anomaly equation (21) shows that $n_{5,\text{eff}}$ is independent of time and so is ξ_B [see Eq. (6)]. This is confirmed in Fig. 5, which shows the temporal evolution of $\langle \xi_B \rangle$.

On the other hand, ξ_B decreases in the nonlinear phase of the simulation runs. From Eq. (14), this results in the increase of λ_{CPI} . This is the origin of the inverse cascade of the magnetic field. Here, as previously reported in Ref. [23], we expect that the decrease of ξ_B ends when $\lambda_{\text{crit}} \sim L$. In Fig. 5, $(2\pi/L)/\xi_{B,\text{ini}}$ is also shown by a solid black line. As we expected, all color lines approach asymptotically the black line after the linear phase. In this way, we can explain the inverse cascade of the magnetic field by the process of the CPI.

Let us look into this mechanism more closely. The evolution of the magnetic field is governed by the induction equation (20), where the second and third terms on the right-hand side are related to the CPI. Here, we evaluate the contribution of the first term to the evolution of the magnetic field. This nonlinear interaction between the fluid and magnetic field is divided into three terms,

$$\nabla \times (v \times B) = B(\nabla \cdot v) + (B \cdot \nabla)v - (v \cdot \nabla)B, \quad (27)$$

which correspond to the compression, stretching, and advection terms, respectively. In Fig. 6, 2D distributions of the y component of the compression [Fig. 6(a)], stretching [Fig. 6(b)], advection [Fig. 6(c)], diffusion [Fig. 6(d)] and CME [Fig. 6(e)] in the induction equation on the x - z plane at $y = 0$, when $t/\tau_{\text{CPI}} = 40$, for model 1 are illustrated. We can see that the first three terms corresponding to the nonlinear interaction are relatively smaller than the last two terms. This indicates that the evolution of the magnetic field in our system is described mostly by the diffusion and CME, which is the process of the CPI.

The condition that the process of the CPI is dominant in the evolution of the magnetic field is derived from the induction equation (20) with a generic current of the form $\Delta \mathbf{J} = \xi_B \mathbf{B}$ [not limited to Eq. (5)] as

$$|\mathbf{v}| \ll \eta |\xi_B|. \quad (28)$$

This condition is indeed satisfied for Eq. (5) with the parameter choice above and $\eta = 1$. Note that this is only the sufficient condition for the inverse cascade. When this condition is not satisfied, then the nonlinear interaction between the fluid and magnetic field is no longer negligible. It would be interesting to study whether the inverse cascade persists in such a case. Finally, in this paper we performed chiral MHD simulations for several given values of ξ_B , but it would also be important to perform self-consistent simulations directly using the form of ξ_B in Eq. (5).

ACKNOWLEDGMENTS

We thank Y. Masada and I. Shovkovy for useful and stimulating discussions. Numerical computations were carried out on Cray XC50 at the Center for Computational Astrophysics, National Astronomical Observatory of Japan and on Yukawa-21 at YITP in Kyoto Univer-

sity. This work was supported by the Keio Institute of Pure and Applied Sciences (KiPAS) project at Keio University, JSPS KAKENHI Grants No. 19K03852 and No. 22H01223 and the Ministry of Science and Technology, Taiwan under Grant No. MOST 110-2112-M-001-070-MY3.

-
- [1] T. D. Lee and C.-N. Yang, Question of Parity Conservation in Weak Interactions, *Phys. Rev.* **104**, 254 (1956).
- [2] C. S. Wu, E. Ambler, R. W. Hayward, D. D. Hoppes, and R. P. Hudson, Experimental Test of Parity Conservation in β Decay, *Phys. Rev.* **105**, 1413 (1957).
- [3] M. Goldhaber, L. Grodzins, and A. W. Sunyar, Helicity of Neutrinos, *Phys. Rev.* **109**, 1015 (1958).
- [4] K. Kotake, K. Sumiyoshi, S. Yamada, T. Takiwaki, T. Kuroda, Y. Suwa, and H. Nagakura, Core-Collapse Supernovae as Supercomputing Science: a status report toward 6D simulations with exact Boltzmann neutrino transport in full general relativity, *PTEP* **2012**, 01A301 (2012), [arXiv:1205.6284 \[astro-ph.HE\]](#).
- [5] A. Burrows, Colloquium: Perspectives on core-collapse supernova theory, *Rev. Mod. Phys.* **85**, 245 (2013), [arXiv:1210.4921 \[astro-ph.SR\]](#).
- [6] T. Foglizzo *et al.*, The explosion mechanism of core-collapse supernovae: progress in supernova theory and experiments, *Publ. Astron. Soc. Austral.* **32**, e009 (2015), [arXiv:1501.01334 \[astro-ph.HE\]](#).
- [7] H. T. Janka, T. Melson, and A. Summa, Physics of Core-Collapse Supernovae in Three Dimensions: a Sneak Preview, *Ann. Rev. Nucl. Part. Sci.* **66**, 341 (2016), [arXiv:1602.05576 \[astro-ph.SR\]](#).
- [8] B. Müller, The Status of Multi-Dimensional Core-Collapse Supernova Models, *Publ. Astron. Soc. Austral.* **33**, e048 (2016), [arXiv:1608.03274 \[astro-ph.SR\]](#).
- [9] D. Radice, E. Abdikamalov, C. D. Ott, P. Mosta, S. M. Couch, and L. F. Roberts, Turbulence in Core-Collapse Supernovae, *J. Phys.* **G45**, 053003 (2018), [arXiv:1710.01282 \[astro-ph.HE\]](#).
- [10] N. Yamamoto, Chiral transport of neutrinos in supernovae: Neutrino-induced fluid helicity and helical plasma instability, *Phys. Rev. D* **93**, 065017 (2016), [arXiv:1511.00933 \[astro-ph.HE\]](#).
- [11] N. Yamamoto and D.-L. Yang, Chiral Radiation Transport Theory of Neutrinos, *Astrophys. J.* **895**, 56 (2020), [arXiv:2002.11348 \[astro-ph.HE\]](#).
- [12] N. Yamamoto and D.-L. Yang, Magnetic field induced neutrino chiral transport near equilibrium, *Phys. Rev. D* **104**, 123019 (2021), [arXiv:2103.13159 \[hep-ph\]](#).
- [13] M. Joyce and M. E. Shaposhnikov, Primordial magnetic fields, right-handed electrons, and the Abelian anomaly, *Phys. Rev. Lett.* **79**, 1193 (1997), [arXiv:astro-ph/9703005](#).
- [14] Y. Akamatsu and N. Yamamoto, Chiral Plasma Instabilities, *Phys. Rev. Lett.* **111**, 052002 (2013), [arXiv:1302.2125 \[nucl-th\]](#).
- [15] A. Vilenkin, Equilibrium parity violating current in a magnetic field, *Phys. Rev.* **D22**, 3080 (1980).
- [16] H. B. Nielsen and M. Ninomiya, The Adler-Bell-Jackiw anomaly and Weyl fermions in a crystal, *Phys. Lett.* **B130**, 389 (1983).
- [17] K. Fukushima, D. E. Kharzeev, and H. J. Warringa, The Chiral Magnetic Effect, *Phys. Rev.* **D78**, 074033 (2008), [arXiv:0808.3382 \[hep-ph\]](#).
- [18] A. Ohnishi and N. Yamamoto, Magnetars and the Chiral Plasma Instabilities, (2014), [arXiv:1402.4760 \[astro-ph.HE\]](#).
- [19] D. Grabowska, D. B. Kaplan, and S. Reddy, Role of the electron mass in damping chiral plasma instability in Supernovae and neutron stars, *Phys. Rev. D* **91**, 085035 (2015), [arXiv:1409.3602 \[hep-ph\]](#).
- [20] M. Dvornikov and V. B. Semikoz, Magnetic field instability in a neutron star driven by the electroweak electron-nucleon interaction versus the chiral magnetic effect, *Phys. Rev. D* **91**, 061301 (2015), [arXiv:1410.6676 \[astro-ph.HE\]](#).
- [21] G. Sigl and N. Leite, Chiral Magnetic Effect in Protoneutron Stars and Magnetic Field Spectral Evolution, *JCAP* **01**, 025, [arXiv:1507.04983 \[astro-ph.HE\]](#).
- [22] N. Yamamoto and D.-L. Yang, Helical magnetic effect and the chiral anomaly, *Phys. Rev. D* **103**, 125003 (2021), [arXiv:2103.13208 \[hep-th\]](#).
- [23] Y. Masada, K. Kotake, T. Takiwaki, and N. Yamamoto, Chiral magnetohydrodynamic turbulence in core-collapse supernovae, *Phys. Rev. D* **98**, 083018 (2018), [arXiv:1805.10419 \[astro-ph.HE\]](#).
- [24] A. Brandenburg, J. Schober, I. Rogachevskii, T. Kahniashvili, A. Boyarsky, J. Fröhlich, O. Ruchayskiy, and N. Kleeorin, The turbulent chiral-magnetic cascade in the early universe, *Astrophys. J. Lett.* **845**, L21 (2017), [arXiv:1707.03385 \[astro-ph.CO\]](#).
- [25] J. Schober, I. Rogachevskii, A. Brandenburg, A. Boyarsky, J. Fröhlich, O. Ruchayskiy, and N. Kleeorin, Laminar and turbulent dynamos in chiral magnetohydrody-

- namics. II. Simulations, *Astrophys. J.* **858**, 124 (2018), [arXiv:1711.09733 \[physics.flu-dyn\]](#).
- [26] T. Miyoshi and K. Kusano, A multi-state HLL approximate Riemann solver for ideal magnetohydrodynamics, *Journal of Computational Physics* **208**, 315 (2005).
- [27] C. R. Evans and J. F. Hawley, Simulation of Magnetohydrodynamic Flows: A Constrained Transport Model, *Astrophys. J.* **332**, 659 (1988).